Function-Based Troposphere Tomography Technique for Optimal Downscaling of Precipitation

Haji-Aghajany, Saeid ; Amerian, Yazdan; Amiri Simkooei, Alireza

Important note
To cite this publication, please use the final published version (if applicable).
Please check the document version above.

Article

Function-Based Troposphere Tomography Technique for Optimal Downscaling of Precipitation

Saeid Haji-Aghajany [1], Yazdan Amerian [1] and Alireza Amiri-Simkooei [2,*]

1 Faculty of Geodesy and Geomatics Engineering, K. N. Toosi University of Technology,
Tehran 1996715433, Iran; s_h_aghajany@mail.kntu.ac.ir (S.H.-A.); amerian@kntu.ac.ir (Y.A.)
2 Department of Geoscience and Remote Sensing, Delft University of Technology,
2600 AA Delft, The Netherlands
* Correspondence: a.amirisimkooei@tudelft.nl

Abstract: Precipitation is an important meteorological indicator that has a direct and significant impact on ecology, agriculture, hydrology, and other vital areas of human health and life. It is therefore essential to monitor variations of this parameter at a global and local scale. To monitor and predict long-term changes in climate elements, Global Circulation Models (GCMs) can provide simulated global-scale climatic processes. Due to the low spatial resolution of these models, downscaling methods are required to convert such large-scale information to regional-scale data for local applications. Among the downscaling methods, the Statistical DownScaling Model (SDSM) and the Artificial Neural Networks (ANNs) are widely used due to their low computational volume and suitable output. These models mainly require training data, and generally, the reanalysis data obtained from the National Center for Environmental Prediction (NCEP) and European Centre for Medium-range Weather Forecasts (ECMWF) are used for this purpose. With an optimal downscaling method, instead of applying the humidity indices extracted from ECMWF data, the outputs of the function-based tropospheric tomography technique obtained from the Global Navigation Satellite System (GNSS) will be used. The reconstructed function-based tropospheric data is then fed to the SDSM and ANN methods used for downscaling. The results of both methods indicate that the tomography can increase the accuracy of the downscaling process by about 20 mm in the wet months of the year. This corresponds to an average improvement of 38% with regard to the root mean square error (RMSE) of the monthly precipitation.

Keywords: precipitation; troposphere tomography; FUNCTION-based; ANN; SDSM

1. Introduction

Today, the rising trend of temperature of the Earth, and variations in the world's climate over time, are known as climate change. Failure to adapt to climate change can have devastating effects on water resources, agriculture, environment, and other aspects of life. Currently, GCMs are the most reliable and widely used products for studying climate change. Although GCM models have proven adequate in predicting the global temperature rise, they have shown very poor behavior in predicting precipitation's behavior and variability [1]. Koutsoyiannis showed that relative humidity has decreased in the last few decades due to the increased temperature, although most GCMs assume it is constant; this is another reason why GCMs are less accurate with regard to the simulation of precipitation [2].

The low spatial resolution of these models reduces their efficiency in local and regional applications such as water resources studies [3]. To provide climatic data with finer spatial resolution, downscaling methods can be used. The existing downscaling methods are classified into two broad categories: the first category uses the statistical relationships of the variables, whereas the second category considers employing their dynamic relationships.

Complete basic information related to these two categories, along with their comprehensive features, can be studied in [3–6].

Among the conventional statistical methods of downscaling, SDSM and Long Ashton Research Station Weather Generator (LARS-WG) models are more widely used due to their simplicity [7–10]. Previous research in statistical downscaling has studied different aspects of this filed. The first group of studies focused on using the statistical and artificial intelligence-based (AI-based) models to detect the relation between the predictands and predictors for a small area. They showed that the SDSM model has a good performance in normal weather conditions [11,12]. The second group used various approaches to choose basic predictors [13,14]. The third group validated the performance of different climate models during statistical downscaling [12,15]. The fourth group worked on integrating the outputs of various models. For example, ref. [16] used Bayesian model averaging (BMA) to combine different regression models.

The regression-based SDSM includes linear and nonlinear experimental relationships between the large-scale climate models and large-scale climate variables as "train" and "predictor" data, respectively, and the small-scale climate variables as "test" data [17,18]. Due to the stochastic nature of precipitation, modeling this process is always a challenge in climatological studies. As a result, methods based on simple regressions may not be successful in modeling and predicting precipitation [19]. It should be noted that in different studies, various methods have been proposed to increase the accuracy of precipitation modeling using various indicators such as long-term persistence, fractal behavior, and intermittency [20,21].

In recent years, ANNs have shown significant success in downscaling precipitation using nonlinear and sometimes complex relationships [22]. ANNs have been also proven useful for precipitation generation and even assessing the performance of models [23,24]. Many researchers used ANN and showed that this technique presents promising output for hydrological downscaling. Some investigators used genetic programming (GP), a hybrid Support Vector Machine with Discrete Wavelet Transform (SVMWT) model, and an ANN to predict precipitation [17,25]. In a recent study, recurrent neural networks (RNNs) have been applied to statistical downscaling, and its advantages were demonstrated, compared against traditional ANNs [26].

Performing the training step, as well as testing both methods, require the use of large-scale climate data. According to previous research, reanalysis data has been the most widely used information for these purposes. Due to the importance of humidity in precipitation modeling, in this paper, instead of using the humidity provided by ECMWF, we use the function-based troposphere tomography outputs along with other climatic parameters extracted from ECMWF reanalysis data.

GNSS tomography is one of the most powerful methods to reconstruct the tropospheric layer [27,28]. In recent years, several studies have been conducted to increase the accuracy of the conventional troposphere tomography, called voxel-based troposphere tomography. For example, Haji-Aghajany and Amerian applied a 3D ray tracing technique to increase the accuracy of ray path reconstruction [29]. They also used a new regularization approach, Weather Research and Forecasting (WRF) model outputs, and the topography of the area, to obtain more accurate results [30,31]. A comprehensive overview of the benefits and deficiencies of current tomography models can be found in [32]. The recently developed method of troposphere tomography is based on basic functions, called function-based troposphere tomography, which has been able to cover some of the weaknesses of voxel-based troposphere tomography and improve it [33,34].

In this study, precipitation is modeled in four different ways: SDSM using ECMWF data (SDSM), SDSM using ECMWF data and tomography results (SDSM-T), ANN using ECMWF data (ANN), and ANN using ECMWF data and tomography results (ANN-T). Finally, the results of different approaches will be objectively compared with each other.

2. Function-Based Troposphere Tomography

The total water vapor content from satellite to receiver, called the Slant Wet Delay (*SWD*) is the most used input data of troposphere tomography and can be computed using [33,35]:

$$SWD = 10^{-6} \int_{Rec.}^{Sat.} N_w ds \tag{1}$$

where N_w is the wet refractivity (mm/km) and s (km) is the path of the signal. The *SWD* (m) is obtained based on Zenith Total Delay (ZTD), Zenith Hydrostatic delay (ZHD), Zenith Wet Delay (ZWD), mapping functions, and delay gradients. More information can be found in the studies [34,36–38].

With voxel-based troposphere tomography, the tomographic area is divided into several voxels. The wet refractivity was considered as a constant in each of the voxels during the specified period of time. For this approach, the equation between the wet refractivity and *SWD* can be discretized as follows [39]:

$$SWD^P = \sum_i^n \sum_j^m \sum_k^q d_{i,j,k}^P N_{(w)i,j,k} \tag{2}$$

where P is the counter of rays, n, m, and q are the numbers of voxels in the latitudinal, longitudinal, and vertical directions, $d_{i,j,k}^P$ is the distance traveled by the signal P in the voxel (i, j, k), and $N_{(w)i,j,k}$ is the wet refractivity in the voxel (i, j, k). Equation (2) can be rewritten in the matrix form as

$$_U L_1 = {}_U A_{n \times m \times q} \; {}_{n \times m \times q} \rho_1 \tag{3}$$

where U is the number of the signals, A is the coefficient matrix, and ρ is a vector, including *SWD*, of each voxel which is unknown. An inversion algorithm needs to be applied to solve the unknown parameters. In this mode of tomography, the coefficient matrix is a large, sparse matrix, and no rays pass through some voxels; therefore, it is impossible to estimate the amount of water vapor in all voxels, thus, introducing different constraints is required to solve this problem [27,39,40]. It is noted that the low accuracy of such constraints will reduce the accuracy of the results.

With function-based troposphere tomography, it is not necessary to divide the tomography area into voxels, and the wet refractivity can be estimated everywhere in the 3D space of the tomographic model. For this method, the area is divided into a number of vertical layers, and the wet refractivity in each layer can be calculated as a function of longitude and latitude (Figure 1).

The *SWD* for the ith layer in the Pth ray direction can be written as [33,34]:

$$SWD_i^P = N_{(w)i} \cdot d_i^P = F(\lambda_i, \varphi_i) \cdot d_i^P \tag{4}$$

where $N_{(w)i}$ is the wet refractivity for the location of (λ_i, φ_i) and d_i^P is the distance traveled by the P-th ray in i-th layer. The total SWD of each ray is equal to the sum of the *SWD* of the ray in each vertical layer. As the spatial distribution of water vapor is not the same at different heights, it is necessary to use the appropriate degree function in each of the vertical levels of the tomography model. Finally, the basic form of the function-based troposphere tomography can be considered as follows [34]:

$$SWD^P = F_1(\lambda_1, \varphi_1) d_1^P + F_2(\lambda_2, \varphi_2) d_2^P + \ldots + F_n(\lambda_n, \varphi_n) d_n^P \tag{5}$$
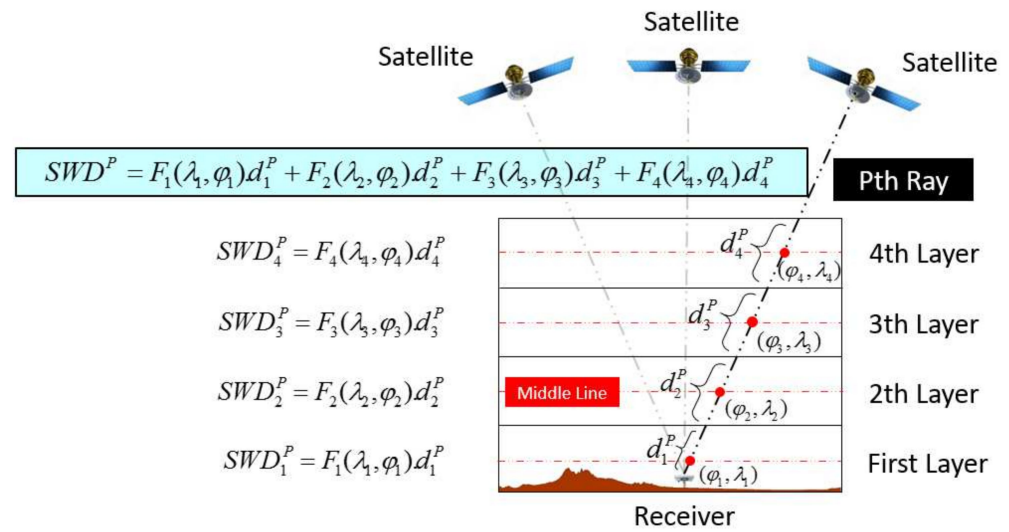
where n is the number of layers.

Figure 1. Sample design of four-layer function-based troposphere tomography [33].

In previous studies, it has been proven that the B-spline function is a powerful tool when modeling the spatial variations of the water vapor. As a result, in this research, various degrees of this function in different vertical layers have been used for the function-based troposphere tomography [33,34]. B-spline is a special kind of wavelet that exhibits useful and remarkable properties such as symmetry, simplicity, semi-orthogonality, and compact support [41]. The 1D B-spline scaling function is as follows:

$$\phi_{J,k}(y) = \frac{y - t_k^J}{t_{k+d}^J - t_k^J} M_{J,k}^{d-1}(y) + \frac{t_{k+d+1}^J - y}{t_{k+d+1}^J - t_{k+1}^J} M_{J,k+1}^{d-1}(y) \tag{6}$$

where d is the degree of function, J is the resolution level, k is shift, y is the variable, M is the normalized B-spline scaling function, $t^J = t_0, t_1, \ldots, t_{K_J+d}$ is a sequence of spaced values called knots, and K_J is the number of basis functions. The 2D B-spline scaling function can be calculated based on the tensor product of 1D functions:

$$\phi_{J_1 J_2 k_1 k_2}(\lambda, \varphi) = \phi_{J_1, k_1}(\lambda) \phi_{J_2, k_2}(\varphi) \tag{7}$$

More details about the B-spline function and its benefits can be found in [42–44]. The wet refractivity in each vertical layer is considered based on the 2D B-spline scaling function $\phi_{J_1 J_2 k_1 k_2}(\lambda_i, \varphi_i)$, with the unknown scaling coefficients $C_{J_1 J_2 k_1 k_2}$ [33,34]:

$$N_{(w)i} = \sum_{k_1=0}^{K_{J_1}-1} \sum_{k_2=0}^{K_{J_2}-1} C_{J_1 J_2 k_1 k_2} \; \phi_{J_1 J_2 k_1 k_2}(\lambda_i, \varphi_i) \tag{8}$$

Finally, the function-based troposphere tomography based on 2D B-spline scaling function is written as follows:

$$SWD^P = (d_1^P \sum_{k_1=0}^{K_{J_1}-1} \sum_{k_2=0}^{K_{J_2}-1} C_{J_1 J_2 k_1 k_2}^1 \; \phi_{J_1 J_2 k_1 k_2}(\lambda_1, \varphi_1)) + \ldots + (d_n^P \sum_{k_1=0}^{K_{J_1}-1} \sum_{k_2=0}^{K_{J_2}-1} C_{J_1 J_2 k_1 k_2}^n \; \phi_{J_1 J_2 k_1 k_2}(\lambda_n, \varphi_n)) \tag{9}$$

which can be written as a matrix relationship between observations and unknowns as:

$$L = Ax \tag{10}$$

where L is the observation vector, A is the coefficient matrix containing the functions and distance traveled by the rays in each vertical layer, and x is an unknown vector including the B-spline scaling coefficients. Finally, the wet refractivity at any point can be

calculated using these coefficients. It should be noted that the obtained wet refractivity can be converted to water vapor pressure and relative humidity based on physical and experimental relationships. Additional information can be studied in [45,46].

The function-based troposphere tomography needs only vertical constraints. More details about this approach can be found in [31,33]. Generally, tomography is a kind of Fredholm integral equation, so it is considered to be an ill-condition problem [47]. In this paper, the least-squares QR (LSQR) iterative regularization method is used to solve the problem [30,47]. The 3D ray-tracing technique is applied to compute the distance traveled by the rays in each vertical layer of the tomographic model [29,48]. More details about 3D ray tracing techniques, its advantages, and its applications in different fields of remote sensing and geodesy can be studied in [29,31,33,49,50].

3. Downscaling Methods

In general, downscaling is performed in two different ways, dynamic and statistical. The models used for dynamic downscaling are similar to GCM, but their temporal and spatial resolution of the network is finer and more accurate. The Regional Climate Model (RegCM) and WRF are among the dynamic models [51]. In the statistical downscaling methods, after determining the optimal function, large-scale climatic variables simulated by GCMs are used as input for these functions [52]. With this method, a statistical correlation using various relations such as simple regression, multiple regression, and ANN is created between the actual behavior of the station and the output of the GCM. After verification, these equations can be used for downscaling future predictions using emission scenarios. SDSM and ANN are two commonly used methods for downscaling based on the statistical relationships [52].

3.1. SDSM

The SDSM is the most widely used method in downsizing climate indicators and was first proposed by [53]. This model is a combination of linear regression and a meteorological stochastic generator, as it uses humidity variables and large-scale, linear silicon patterns in the atmosphere that generate meteorological indices at the local scale. The occurrence of precipitation is a conditional process and is modeled on predictor variables using a conditioned meteorological generator [54]:

$$w_t = a_0 + \sum_{j=1}^{n} a_j \hat{u}_t^j \tag{11}$$

where w_t is the conditional probability of precipitation, a is the regression parameter obtained by the least squares method, u_t^j is the j-number predictor variable on day t, and n is number of predictor parameters. In the second step, the estimated amount of precipitation per rainy day is determined [53]:

$$Z_t = \beta_0 + \sum_{j=1}^{n} \beta_j \hat{u}_t^j + \varepsilon \tag{12}$$

where β is the regression parameter. Finally, precipitation for day t can be determined as

$$Y_t = F^{-1}[\phi(Z_t)] \tag{13}$$

where F is the experimental function and ϕ is the normal cumulative distribution function. During this process, many errors are adjusted to bring the observed and simulated variables closer together.

In the SDSM, after setting-up and the quality control of observations is complete, statistical downscaling is performed, using local-scale station data for testing, and large-scale data for prediction and training.

3.2. ANNs

An ANN is a data processing approach that has analogous efficiency to the biological neural networks of the human brain [55]. The Multi-Layer Perceptrons (MLPs) are the simplest and most popular mode of an ANN. These modes are widely used to make connections between input and output information [56]. MLPs are feed-forward networks which contain one or more hidden layers. A MLP is a user-friendly algorithm that allows you to estimate any relationship between inputs and outputs using training algorithms [57]. The Levenberg–Marquardt (LM) training algorithm, along with the Gradient Descent (GD), Broyden–Fletcher–Goldfarb–Shanno (BFGS), and Conjugate Gradient Fletcher-Reeves Update (CGF) methods, have been successfully used in various investigations to train MLP networks [58–61].

The LM algorithm [58,59] is a powerful learning method for MLP feed-forward networks. This algorithm is a modified version of the classic Newton algorithm for calculating a suitable answer to the optimization problem. This algorithm uses an approximation of the Hessian matrix:

$$\mathbf{X}_{k+1} = \mathbf{X}_k - [\underbrace{\mathbf{J}^{\mathrm{T}}\mathbf{J} + \mu\mathbf{I}}_{\mathbf{H}}]^{-1}\mathbf{J}^{\mathrm{T}}\mathbf{e} \tag{14}$$

where X is the weight, J is the efficiency criteria Jacobian matrix, e is the residual vector, and μ is the combination coefficient, which is always positive, thus making H positive, definite, and invertible.

In the neural network model, the data are divided into two categories: training and testing. In this method, the weight of connections is determined in such a way that by applying each input series of network training data, it can produce the corresponding output with a specific error. After training the network, test data are used to evaluate the trained network. In ANNs, a stimulus function such as a linear, sigmoid log, and similar functions, are used to transfer the output of each layer to the next layer. Figure 2 shows the steps of downscaling the precipitation process using ANN.

An efficient neural network requires proper architecture. This optimal architecture depends on the data set and their properties. The number of neurons in the input and output layers is determined based on the number of inputs and outputs of the network. There is no specific basis for the number of neurons in the middle layers, and it is generally determined by a trial-and-error method.
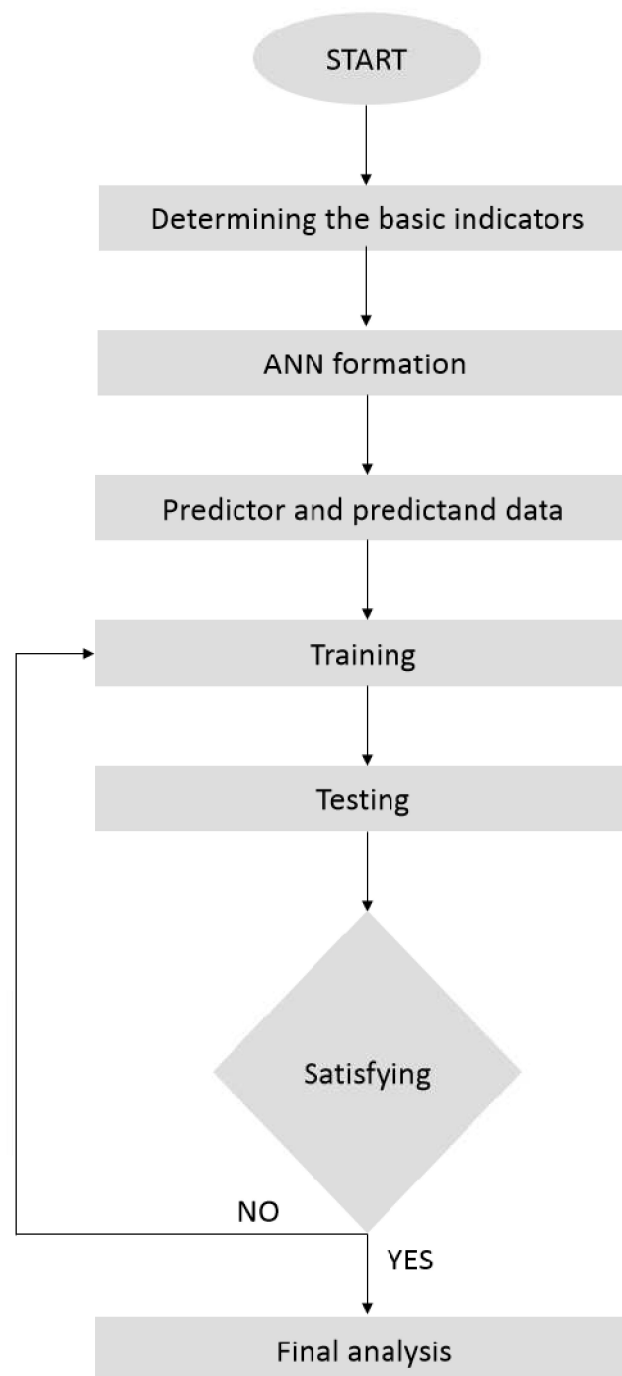
Figure 2. Downscaling algorithm using ANN.

4. Validation Methods

Generally, to validate and to compare the efficiency of various downscaling methods, statistical indices including the Root Mean Square Error (*RMSE*), Nash-Sutcliffe Efficiency (*NSE*), determination coefficient (R^2), and Mean Absolute Error (*MAE*), are used. These indices are computed, respectively, as follows [62]:

$$RMSE = [\frac{1}{n}\sum_{i=1}^{n}(S_i - O_i)^2]^{\frac{1}{2}} \tag{15}$$

$$NSE = 1 - \frac{\sum\limits_{i=1}^{n}(O_i - S_i)^2}{\sum\limits_{i=1}^{n}(O_i - \overline{O})^2} \tag{16}$$

$$R^2 = \left[\frac{\frac{1}{n}\sum\limits_{i=1}^{n}(S_i - \overline{S})(O_i - \overline{O})}{\sigma_s \times \sigma_o}\right]^2 \tag{17}$$

$$MAE = \frac{\sum\limits_{i=1}^{n}|S_i - O_i|}{n} \tag{18}$$

where S_i and O_i are the modeled and observed data, $\overline{S}$ and $\overline{O}$ are the average of the modeled and observed data, and σ_o and σ_s are the standard deviation of the modeled and observed data, respectively. RMSE is used to validate the predictive power of various models. R^2 indicates the relationship between the modeled and observed data. The range of changes in this index is between zero and one. If it is equal to one, it indicates a strong relationship between the two inputs.

5. Study Area and Data Set

An area in North America has been selected to perform the methodology proposed. Measurements of 72 Global Positioning System (GPS) stations under various weather conditions and different topographies from 1995 to 2020 have been used for troposphere tomography. The distribution of the stations on the background of the topography can be seen in Figure 3. Not all stations are used at all epochs because of the lack of data in some stations at those epochs. The obtained results were validated using available radiosonde stations in the area. Radiosonde observations can measure atmospheric pressure, air-temperature, and relative humidity observations accurately; therefore, the use of this instrument is one of the most common methods to validate the outputs of troposphere tomography. The radiosonde data can be received for free form National Oceanic and Atmospheric Administration (NOAA). The location of the radiosonde station can also be seen in Figure 3.
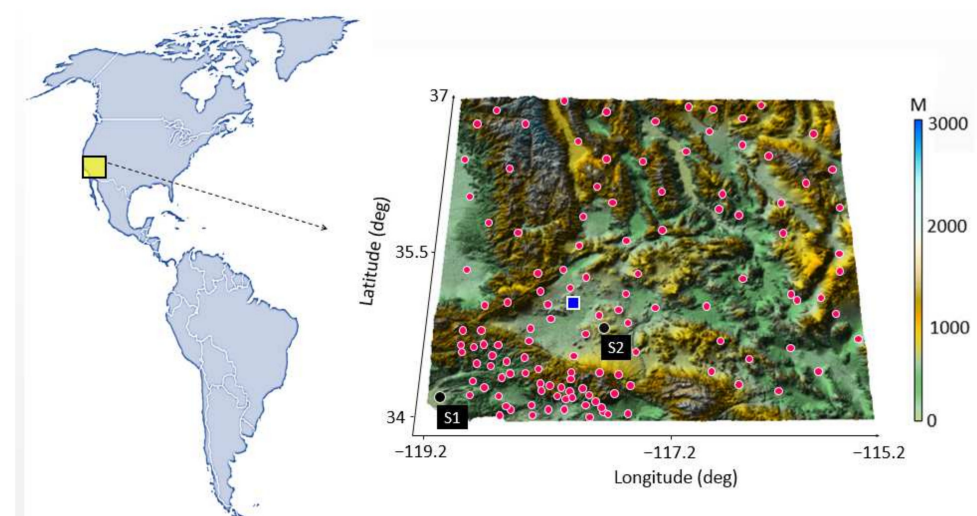

Figure 3. Distribution of GNSS stations and topography of the area. The blue square shows the location of the radiosonde station, red circles show the GNSS stations, and black circles show the position of the stations where precipitation downscaling took place.

In this research, two different types of meteorological data have been used. The first type is the ERA5 reanalysis data from ECMWF that have been used as large-scale meteorological information for calibrating and evaluation, covering from 1950 to the present. It provides values of the climate data on 37 pressure levels, with a spatial resolution of about 31 km [63]. This data has also been used to perform a 3D ray tracing technique for troposphere tomography. Previous research has proven that reanalysis data is very useful and applicable in different fields, including remote sensing, geodynamics, and geodesy [64–66].

The second type of data is the daily precipitation data from two synoptic stations including Station1 (S1) and Station2 (S2) in different precipitation conditions for the period of 1995 to 2020; it is used as predictand data (Figure 3). Figure 4 shows the quad-daily (6-h) total precipitation of two selected stations from ERA5 data for a period of 27 years. The difference in the precipitation conditions at the two stations is quite visible. The difference in total precipitation between these two stations may be due to the higher altitude of S2. The proximity of this station to the sea is also one of the reasons that should be considered.
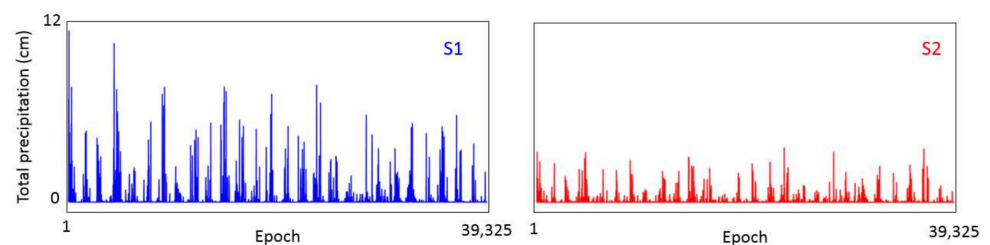
Figure 4. Quad-daily (six h) precipitation at the location of two selected stations S1 and S2 from January 1995 to December 2021, extracted from ERA5 data.

6. Processing Results and Discussions

Figure 5 shows the steps of precipitation downscaling using SDSM, ANN, and tomography techniques.

Figure 5. A simple process flowchart of this study.

The processes of this research are classified into three separate parts: the first part is related to the tomography and reconstruction of water vapor and its evaluation; the second

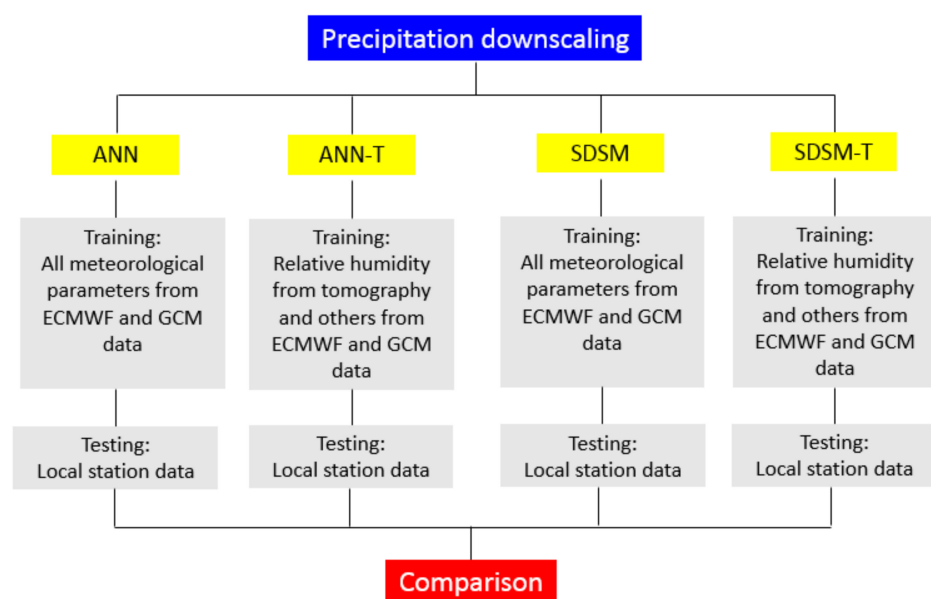part includes the downscaling of the precipitation process using the proposed methods; and the last part is related to the final evaluation of the results using statistical formulas.

6.1. Troposphere Tomography

Selecting the optimal degree and level of the B-spline function is the first step in function-based tomography. Due to the altitude changes of water vapor in the troposphere, it is necessary to consider different degrees and levels of function at different height levels of the tomographic model. The ERA5 reanalysis data has been applied to determine the suitable degree and level at different vertical levels. Different degrees and levels of the B-spline functions were fitted to one year of the reanalysis data, and the coefficient of the B-spline functions were calculated. The reanalysis data of 20 days in various weather conditions were considered in order to validate the results of the B-spline function at different vertical levels. The skeleton of the considered tomographic model, together with the intended degrees and levels for the B-spline function in each vertical layer, can be seen in Figure 6. Based on intensive experimental tests, the vertical resolution proposed in this figure was found to provide the most accurate results compared with other settings.
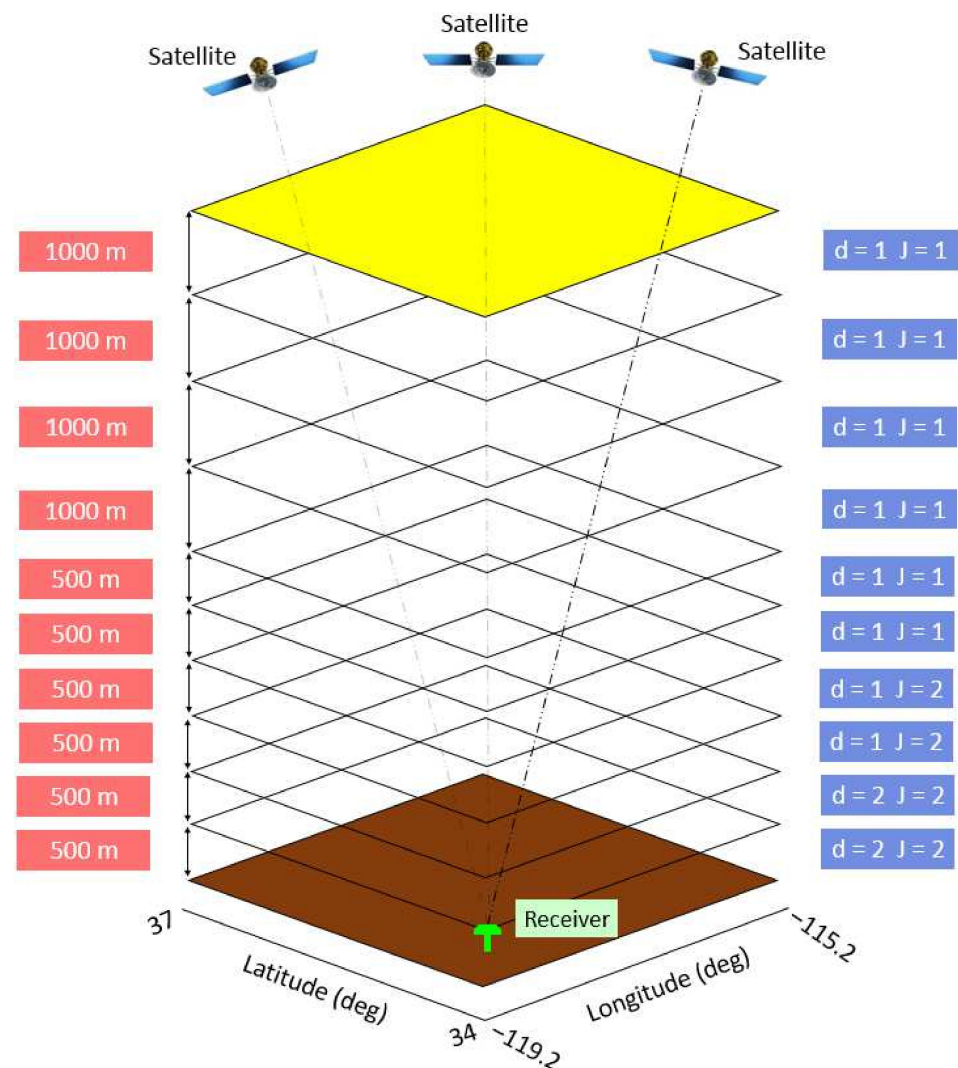

Figure 6. Tomography model together with a schematic diagram of considered degrees and levels at different vertical layers.

The GPS measurements were processed using Bernese 5.2 software to compute the ZTD [67]. The ionospheric-free linear combination, the ZTD with a 6-h temporal resolution,

and the gradients in the east–west and north–south directions with a 12 h temporal resolution, have been selected for this processing. The global mapping function (GMF), based on the Global Pressure Temperature model (GPT), has been applied to project the zenith direction to the slant direction [68].

After performing all the necessary processing, the wet refractivity was reconstructed in different epochs. Figure 7 shows examples of the reconstructed wet refractivity in four different epochs. After reconstructing the refractivity, we needed to validate the outputs using the radiosonde measurements. Samples of this validation for the four different epochs are shown in Figure 8. Although there are differences between the outputs and radiosonde observations at some vertical levels, it can be observed that the reconstructed wet refractivity is generally consistent with validation data. Statistical measures have been used for a better comparison (Table 1).
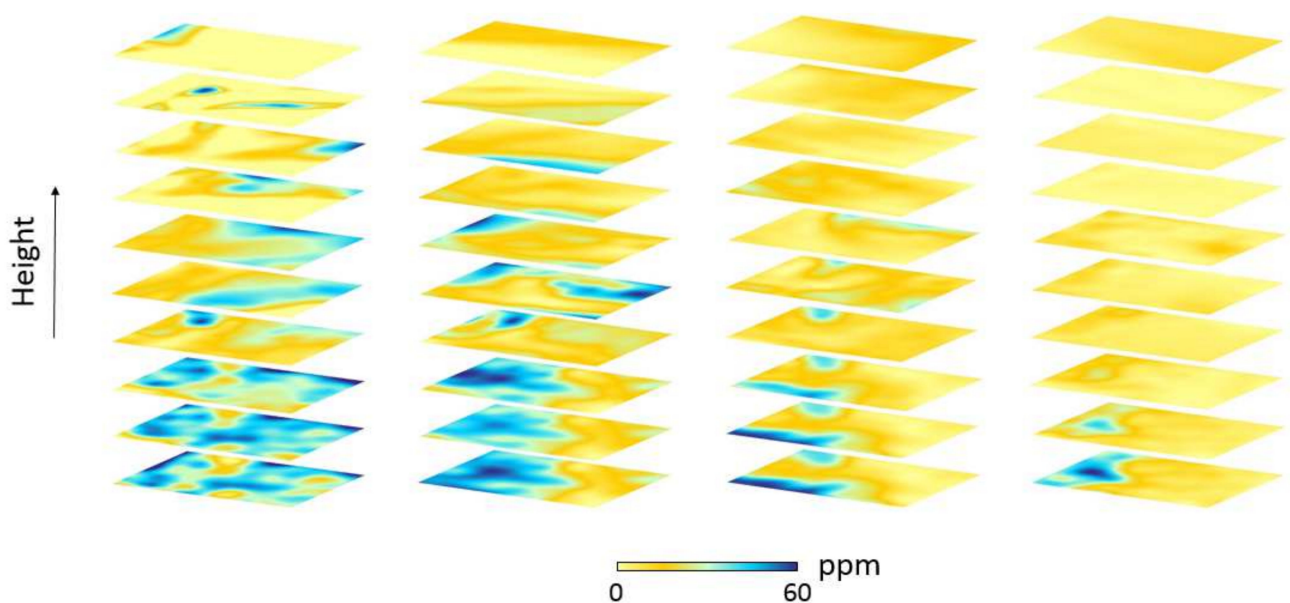
Figure 7. Samples of reconstructed wet refractivity field at epochs 14,124, 14,484, 14,844, and 15,204, from left to right.
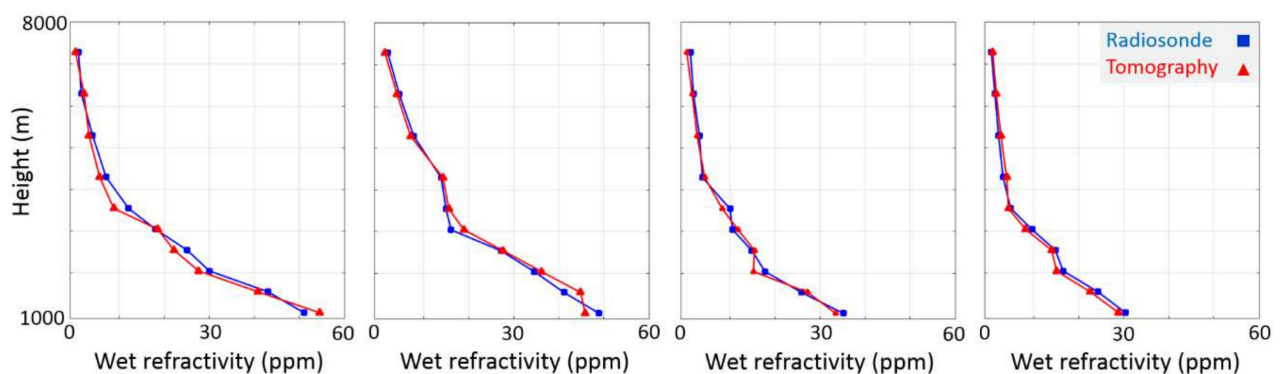
Figure 8. Comparison of wet refractivity to the profile derived from radiosonde observations in epochs 14,124, 14,484, 14,844, and 15,204, from left to right.

Table 1. The statistical measures between the validation data and outputs over the processing period.

RMSE (ppm)	Bias (ppm)	Min-Diff (ppm)	Max-Diff (ppm)
2.26	0.46	0.09	5.78

These statistics, especially RMSE, show that the reconstructed wet refractivity is satisfactorily consistent with the radiosonde measurements.

6.2. Downscaling of Precipitation Based on the SDSM

With this method, first, the daily data of the synoptic stations are qualitatively controlled. After quality control, the best parameters are selected based on statistical analysis from the available variables to predict the precipitation process. The meteorological data for the period 1995–2020 have been divided into two parts: 1995–2015 and 2016–2020. The first part has been used for model training, whereas the second part has been used for model testing, as an independent set of information. Humidity plays an important role in predicting precipitation in climatological studies; therefore, this paper focuses on examining the role of using accurate value of humidity in predicting precipitation.

All processes have been performed in two different modes: the first mode uses the ERA5 data (SDSM), and the second mode uses the humidity obtained from the tomography, instead of that provided by ERA5 data, along with other indicators of ERA5 (SDSM-T). We also note that on the dates when GPS observations were not available for tomography, the humidity obtained from ERA5 was used. This problem happened on 143 different days during the processing time. The statistical analysis, at both stations, showed that the predominant predictors for the precipitation process are the average sea level pressure, geopotential height, 2 m temperature, and relative humidity at some pressure levels. It was also observed that in the SDSM-T mode, the correlation between humidity and precipitation is higher than the SDSM. The correlation coefficient between the predictor and predictant for the SDSM mode can be seen in Figure 9.
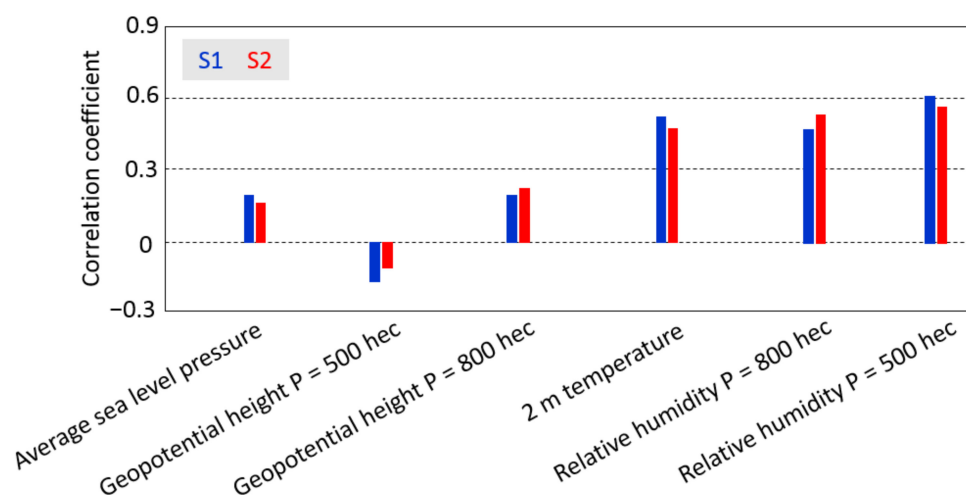

Figure 9. Correlation coefficient between the meteorological parameters and precipitation for the SDSM mode at the two selected stations.

After selecting the six variables mentioned in Figure 9, the training process and testing of both processing modes are performed.

6.3. Downscaling of Precipitation Based on an ANN

As mentioned, six indicators were considered as the main parameters, and thus, the input for the MLP neural network. In the next step, it was necessary to select the optimal training algorithm for the neural network. For this purpose, the neural network has been trained using widely known algorithms, of which their results have been provided in Table 2. As the values of the determination coefficient are always between 0 and 1, the decision based on this coefficient is simple, and it may seem that this coefficient can be a suitable criterion for evaluation; however, this coefficient cannot be a suitable criterion if used alone, because in a hypothetical model, it is possible that the modeled values and

observations are very different, but the errors are such that they follow a uniform trend. In this case, the value of the determination coefficient will be misleading. For this reason, in addition to this coefficient, other statistical indicators have been used for evaluation. Based on Table 2, it can be concluded that the LM algorithm is the most suitable option for building an optimal neural network.

Table 2. Statistical indicators related to the use of various training functions for S1 and S2.

Training Algorithm	S1			S2		
	RMSE	NSE	R^2	RMSE	NSE	R^2
GD	7.412	0.178	0.746	7.98	0.311	0.846
LM	0.368	0.954	0.972	0.399	0.961	0.942
BFGS	0.521	0.924	0.911	0.475	0.901	0.881
CGF	0.784	0.913	0.831	0.739	0.919	0.883

After selecting the optimal training algorithm, it is time to determine the optimal number of layers and neurons. For this purpose, based on the trial-and-error method, the neural network has been implemented in various situations. Examples of the obtained results can be seen in Table 3.

Table 3. Examples of results obtained from the use of a different number of layers and neurons for S1.

Model Number	Number of Hidden Layers	Number of Neurons in the First Layer	Number of Neurons in the Second Layer	RMSE	NSE	R^2
1	1	2	-	0.597	0.953	0.891
2	1	6	-	0.574	0.942	0.893
3	1	12	-	0.458	0.962	0.898
4	1	18	-	0.524	0.949	0.889
5	2	2	2	0.584	0.954	0.898
6	2	4	6	0.612	0.963	0.901
7	2	6	8	0.574	0.951	0.902
8	2	8	8	0.404	0.964	0.901
9	2	10	10	0.531	0.943	0.914
10	2	14	8	0.438	0.963	0.891

Based on the results presented in Table 3, it can be concluded that the use of two hidden layers with eight neurons in each layer can create an optimal ANN. The processes related to the other station showed the same result. It should be noted that the tangent and sigmoid log activation functions have been used for the hidden layers, and the linear activation function has been used for the output layer. Finally, the characteristics of the optimal ANN are given in Table 4.

Table 4. Characteristics of the ANN in this study.

ANN Type	Number of Neurons	Stimulus Function of Hidden Layers	Stimulus Function of Output Layers	Training Algorithm
Three-layer feed-forward MLP	8-8	tangent and sigmoid log	Linear	LM

6.4. Validation and Discussions

After performing the calibration step in the SDSM model, and thus, preparing the optimal ANN, it is necessary to compare the results of these two models with the observations of the two stations during the evaluation period from 2016 to 2020. For a fairer comparison, the results obtained for each month have been compared with the observations of that month, because it is expected that, in more rainy months, there will be a more significant difference between the results. Figure 10 shows the determination coefficient between observations and obtained precipitation from the different modes.

Figure 10. Determination coefficient between observations and modeled daily precipitation.

A comparison of the results obtained from the determination coefficient shows that in general, the values obtained from different methods are consistent with the observations. This adaptation is greater in the months with less rainfall. In wet months, such as November, December, January, and February, the determination coefficient is reduced. In the entire year, however, the use of the tomography technique led to improved results and the coefficient increased. The highest coefficient belongs to the ANN-T mode. The results obtained from the SDSM model and the ANN are close to each other, regardless of whether the tomographic results are used or not. As mentioned before, in order to compare and draw better conclusions, it is necessary to check other statistical indicators.

Figure 11 shows the average monthly precipitation MAE obtained from different modes for the two stations. The MAE shows the power of the tomography technique in improving the accuracy of the downscaling process. As can be seen, the improvement in the accuracy of the results, when tomography is used, is quite noticeable across almost all months. This becomes even more noticeable during the wet months of the year. Moreover, in the first station, as it has more precipitation than the second station, the difference between the results is greater. The results of January, November, and December clearly show the role of the tomography technique in the downscaling process. In some months, such as June and July, which are the dry months, the results are very close to each other. In January, the use of tomographic results has led to the improvement of the accuracy of the ANN method by about 11 mm and 9 mm in the first and second stations, respectively. In addition, in the same month, the improvement of the result of the SDSM method, when using tomography, is about 13 mm and 8 mm in the first and second stations, respectively. Such an improvement in the accuracy of the results is significant and shows the efficiency of the tomography technique. The results obtained from the first station in November and December also emphasize that the use of accurate methods, such as tomography, can increase the accuracy of widely used models of downscaling by about one centimeter. Similarly to the determination coefficient, these results also show that the highest accuracy belongs to the ANN-T mode, although the values of the ANN-T and SDSM-T modes are

close to each other, and in some months, such as May and June, they are almost identical. For a more comprehensive comparison, MAE and RMSE have also been examined. Table 5 shows the RMSE for different methods.
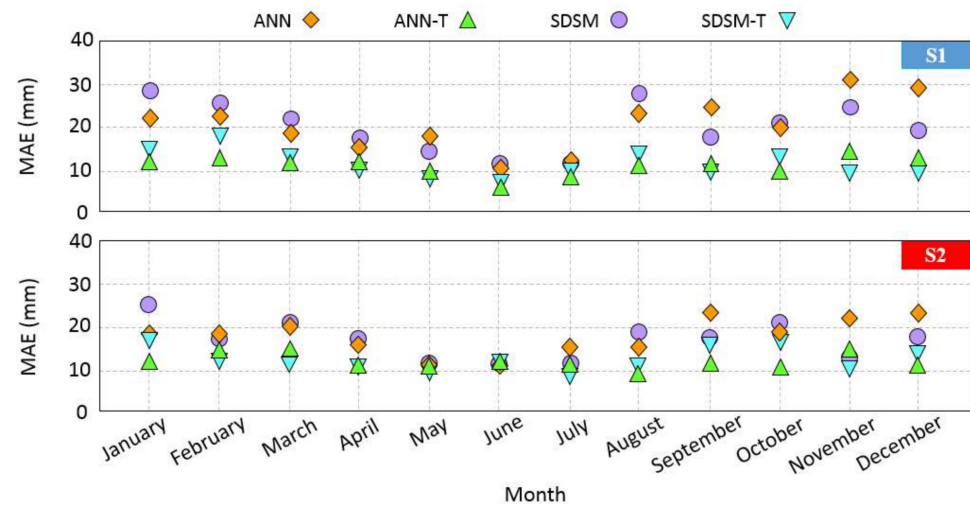

Figure 11. Average monthly precipitation MAE from 2016 to 2020.

Table 5. Obtained RMSE for each mode (the best results of each month are highlighted in green).

Indicator	Month	S1				S2			
		ANN	ANN-T	SDSM	SDSM-T	ANN	ANN-T	SDSM	SDSM-T
RMSE (mm)	January	29.24	11.47	30.12	15.87	17.69	10.84	25.51	18.08
	February	20.15	14.34	23.57	17.66	28.29	12.43	29.52	15.68
	March	27.36	13.74	24.89	13.42	20.91	13.28	23.64	14.27
	April	17.58	10.43	23.74	14.08	15.94	10.07	14.51	11.87
	May	19.46	14.84	17.49	16.19	16.83	11.92	15.03	11.27
	June	12.81	10.45	10.74	09.86	11.83	10.93	12.39	12.84
	July	13.87	11.43	15.76	14.79	13.24	12.51	14.84	13.63
	August	31.47	18.23	32.11	21.63	21.52	11.36	23.87	13.96
	September	33.88	14.21	24.31	16.75	26.82	13.87	22.26	12.73
	October	26.89	17.28	30.05	21.49	23.83	15.86	25.74	12.18
	November	38.23	16.71	35.61	20.72	27.84	18.42	20.68	18.91
	December	32.39	16.34	25.46	18.53	28.93	19.88	26.79	16.64
Average (mm)	All months	25.27	14.12	24.48	16.74	21.13	13.14	21.23	14.33

The RMSE shown in this table indicates the strength of the tomography technique in increasing the accuracy of the results, similarly to the previous statistical indicators. The ANN-T and SDSM-T results are generally close to each other, but it can be said that the ANN-T method has a better performance in the precipitation modeling. The largest difference between the ANN-T and SDSM-T is observed in January, and in the second station, which reaches 8 mm. The greatest improvement in ANN-T accuracy is observed in January, September, and November, when the improvement reaches about 20 mm. This is also true for the SDSM-T method. The rate of improvement of the results due to the use of tomography reaches about 15 mm.

It can be concluded that the ANN-T mode is the most suitable option for the downscaling process. Of course, this issue, to a large extent, depends on choosing an optimal network whose steps were mentioned in the previous sections.

7. Conclusions

This paper focused on examining the impact of using an accurate and modern function-based troposphere tomography technique for the process of downscaling the precipitation process. For this purpose, the widely used ANN and SDSM methods were studied. After specifying the study area, two synoptic stations with different precipitation conditions in the area were selected. First, the tomography process was performed during the testing period and the results were evaluated using the radiosonde observations. In the next stage, the processing time was divided into two parts: the first part was for training and the second part was for testing the models. ERA5 data published by ECMWF were used to perform downscaling. Due to the significant effect of humidity in precipitation downscaling, instead of applying the humidity proposed by ERA5 data, function-based troposphere tomography results were used along with other indexes extracted from ERA5 reanalysis data. Processes were accomplished in four different modes: SDSM, SDSM-T, ANN, and ANN-T. In the first step, the SDSM model was trained, and the setting of the optimal ANN were specified. Then, the results obtained from the four modes during the evaluation period were compared with the synoptic observations. The results showed that the use of tomography can reduce the RMSE by about 20 mm in the wet months of the year. Moreover, based on the results, it can be concluded that, in general, the results of the ANN-T and SDSM-T modes are close to each other, especially in the dry months of the year. The combination of the ANN method and the tomography technique can lead to the most accurate results.

Conflicts of Interest: The authors declare no conflict of interest.

References

1. Anagnostopoulos, G.G.; Koutsoyiannis, D.; Christofides, A.; Efstratiadis, A.; Mamassis, N. A comparison of local and aggregated climate model outputs with observed data. *Hydrol. Sci. J.* **2010**, *55*, 1094–1110. [CrossRef]
2. Koutsoyiannis, D. Revisiting the global hydrological cycle: Is it intensifying? *Hydrol. Earth Syst. Sci.* **2020**, *24*, 3899–3932. [CrossRef]
3. Hewitson, B.C.; Crane, R.G. Climate downscaling: Techniques and application. *Clim. Res.* **1996**, *7*, 85–95. [CrossRef]
4. Xu, C.Y. From GCMs to river flow: A review of downscaling methods and hydrologic modelling approaches. *Prog. Phys. Geogr. Earth Environ.* **1999**, *23*, 229–249. [CrossRef]
5. Wilby, R.L.; Charles, S.P.; Zorita, E.; Timbal, B.; Whetton, P.; Mearns, L.O. Guidelines for Use of Climate Scenarios Developed from Statistical Downscaling Methods. Supporting Material of the Intergovernmental Panel on Climate Change. The DDC of IPCC TGCIA 27. 2004. Available online: https://www.semanticscholar.org/paper/Guidelines-for-Use-of-Climate-Scenarios-Developed-Wilby-Charles/3f10e91a922860e49a42b4ee5ffa11ad7e6500e8 (accessed on 7 May 2022).
6. Fowler, H.J.; Blenkinsop, S.; Tebaldi, C. Linking climate change modelling to impacts studies: Recent advances in downscaling techniques for hydrological modelling. *Int. J. Climatol.* **2007**, *27*, 1547–1578. [CrossRef]
7. Semenov, M.A.; Brooks, R.J.; Barrow, E.M.; Richardson, C.W. Comparison of the WGEN and LARS-WG stochastic weather generators for diverse climates. *Clim. Res.* **1998**, *10*, 95–107. [CrossRef]
8. Dibike, Y.B.; Coulibaly, P. Hydrologic impact of climate change in the Saguenay watershed: Comparison of downscaling methods and hydrologic models. *J. Hydrol.* **2005**, *307*, 145–163. [CrossRef]
9. Kilsby, C.G.; Jones, P.D.; Burton, A.; Ford, A.C.; Fowler, H.J.; Harpham, C.; James, P.; Smith, A.; Wilby, R.L. A daily weather generator for use in climate change studies. *Environ. Model. Softw.* **2007**, *22*, 1705–1719. [CrossRef]
10. Kim, B.S.; Kim, H.S.; Seoh, B.H.; Kim, N.W. Impact of climate change on water resources in Yongdam Dam Basin, Korea. *Stoch. Environ. Res. Risk Assess.* **2007**, *21*, 355–373. [CrossRef]

11. Chen, S.-T.; Yu, P.-S.; Tang, Y.-H. Statistical downscaling of daily precipitation using support vector machines and multivariate analysis. *J. Hydrol.* **2010**, *385*, 13–22. [CrossRef]

12. Li, X.; Li, Z.; Huang, W.; Zhou, P. Performance of statistical and machine learning ensembles for daily temperature downscaling. *Arch. Meteorol. Geophys. Bioclimatol. Ser. B* **2020**, *140*, 571–588. [CrossRef]

13. Hammami, D.; Lee, T.S.; Ouarda, T.B.M.J.; Lee, J. Predictor selection for downscaling GCM data with LASSO. *J. Geophys. Res. Earth Surf.* **2012**, *117*, 211–226. [CrossRef]

14. Nourani, V.; Razzaghzadeh, Z.; Baghanam, A.H.; Molajou, A. ANN-based statistical downscaling of climatic parameters using decision tree predictor screening method. *Arch. Meteorol. Geophys. Bioclimatol. Ser. B* **2018**, *137*, 1729–1746. [CrossRef]

15. Singh, V.; Jain, S.K.; Singh, P.K. Inter-comparisons and applicability of CMIP5 GCMs, RCMs and statistically downscaled NEXGDDP based precipitation in India. *Sci. Total Environ.* **2019**, *697*, 134163. [CrossRef] [PubMed]

16. Su, H.; Xiong, Z.; Yan, X.; Dai, X. An evaluation of two statistical downscaling models for downscaling monthly precipitation in the Heihe River basin of China. *Arch. Meteorol. Geophys. Bioclimatol. Ser. B* **2019**, *138*, 1913–1923. [CrossRef]

17. Heyen, H.; Zorita, E.; Von Storch, H. Statistical downscaling of monthly mean North Atlantic air-pressure to sea level anomalies in the Baltic Sea. *Tellus A Dyn. Meteorol. Oceanogr.* **1996**, *48*, 312–323. [CrossRef]

18. Wilby, R.L.; Dawson, C.W.; Barrow, E.M. SDSM—A decision support tool for the assessment of regional climate change impacts. *Environ. Model. Softw.* **2002**, *17*, 145–157. [CrossRef]

19. Iliopoulou, T.; Koutsoyiannis, D. Projecting the future of rainfall extremes: Better classic than trendy. *J. Hydrol.* **2020**, *588*, 125005. [CrossRef]

20. Lombardo, F.; Volpi, E.; Koutsoyiannis, D. Rainfall downscaling in time: Theoretical and empirical comparison between multifractal and Hurst-Kolmogorov discrete random cascades. *Hydrol. Sci. J.* **2012**, *57*, 1052–1066. [CrossRef]

21. Dimitriadis, P.; Koutsoyiannis, D.; Iliopoulou, T.; Papanicolaou, P. A Global-Scale Investigation of Stochastic Similarities in Marginal Distribution and Dependence Structure of Key Hydrological-Cycle Processes. *Hydrology* **2021**, *8*, 59. [CrossRef]

22. Kourgialas, N.N.; Dokou, Z.; Karatzas, G.P. Statistical analysis and ANN modeling for predicting hydrological extremes under climate change scenarios: The example of a small Mediterranean agro-watershed. *J. Environ. Manag.* **2015**, *154*, 86–101. [CrossRef] [PubMed]

23. Rozos, E.; Dimitriadis, P.; Mazi, K.; Koussis, A. A Multilayer Perceptron Model for Stochastic Synthesis. *Hydrology* **2021**, *8*, 67. [CrossRef]

24. Rozos, E.; Dimitriadis, P.; Bellos, V. Machine Learning in Assessing the Performance of Hydrological Models. *Hydrology* **2021**, *9*, 5. [CrossRef]

25. Shenify, M.; Danesh, A.S.; Gocić, M.; Taher, R.S.; Wahab, A.W.A.; Gani, A.; Shamshirband, S.; Petković, D. Precipitation Estimation Using Support Vector Machine with Discrete Wavelet Transform. *Water Resour. Manag.* **2015**, *30*, 641–652. [CrossRef]

26. Wang, Q.; Huang, J.; Liu, R.; Men, C.; Guo, L.; Miao, Y.; Jiao, L.; Wang, Y.; Shoaib, M.; Xia, X. Sequence-based statistical downscaling and its application to hydrologic simulations based on machine learning and big data. *J. Hydrol.* **2020**, *586*, 124875. [CrossRef]

27. Flores, A.; Ru_ni, G.; Rius, A. 4D tropospheric tomography using GPS slant wet delays. *Ann. Geophys.* **2000**, *18*, 223–234. [CrossRef]

28. Rohm, W.; Bosy, J. Local tomography troposphere model over mountains area. *Atmos. Res.* **2009**, *93*, 777–783. [CrossRef]

29. Aghajany, S.H.; Amerian, Y. Three dimensional ray tracing technique for tropospheric water vapor tomography using GPS measurements. *J. Atmos. Sol. Terr. Phys.* **2017**, *164*, 81–88. [CrossRef]

30. Haji-Aghajany, S.; Amerian, Y. Hybrid Regularized GPS Tropospheric Sensing Using 3-D Ray Tracing Technique. *IEEE Geosci. Remote Sens. Lett.* **2018**, *15*, 1475–1479. [CrossRef]

31. Haji-Aghajany, S.; Amerian, Y.; Verhagen, S.; Rohm, W.; Ma, H. An Optimal Troposphere Tomography Technique Using the WRF Model Outputs and Topography of the Area. *Remote Sens.* **2020**, *12*, 1442. [CrossRef]

32. Brenot, H.; Rohm, W.; Kačmařík, M.; Möller, G.; Sá, A.; Tonda´s, D.; Rapant, L.; Biondi, R.; Manning, T.; Champollion, C. Cross-Comparison and Methodological Improvement in GPS Tomography. *Remote Sens.* **2019**, *12*, 30. [CrossRef]

33. Haji-Aghajany, S.; Amerian, Y.; Verhagen, S. B-spline function-based approach for GPS tropospheric tomography. *GPS Solut.* **2020**, *24*, 88. [CrossRef]

34. Haji-Aghajany, S.; Amerian, Y.; Verhagen, S.; Rohm, W.; Schuh, H. The effect of function-based and voxel-based tropospheric tomography techniques on the GNSS positioning accuracy. *J. Geod.* **2021**, *95*, 78. [CrossRef]

35. Braun, J.J. Remote Sensing of Atmospheric Water Vapor with the Global Positioning System. Ph.D. Thesis, University of Colorado, Boulder, CO, USA, 2004.

36. Bevis, M.; Businger, S.; Herring, T.A.; Rocken, C.; Anthes, R.A.; Ware, R.H. GPS meteorology: Remote sensing of atmospheric water vapor using the global positioning system. *J. Geophys. Res. Atmos.* **1992**, *97*, 15787–15801. [CrossRef]

37. Davis, J.; Elgered, G.; Niell, A.E.; Kuehn, C.E. Ground-based measurement of gradients in the "wet" radio refractivity of air. *Radio Sci.* **1993**, *28*, 1003–1018. [CrossRef]

38. Chen, B.Y.; Liu, Z.Z. Voxel-optimized regional water vapor tomography and comparison with radiosonde and numerical weather model. *J. Geod.* **2014**, *88*, 691–703. [CrossRef]

39. Troller, M.; Bürki, B.; Cocard, M.; Geiger, A.; Kahle, H.-G. 3-D refractivity field from GPS double difference tomography. *Geophys. Res. Lett.* **2002**, *29*, 2-1–2-4. [CrossRef]

40. Bender, M.; Dick, G.; Ge, M.; Deng, Z.; Wickert, J.; Kahle, H.-G.; Raabe, A.; Tetzlaff, G. Development of a GNSS water vapour tomography system using algebraic reconstruction techniques. *Adv. Space Res.* **2011**, *47*, 1704–1720. [CrossRef]

41. Amerian, Y.; Hossainali, M.M.; Voosoghi, B. Regional improvement of IRI extracted ionospheric electron density by compactly supported base functions using GPS observations. *J. Atmos. Sol. Terr. Phys.* **2013**, *92*, 23–30. [CrossRef]

42. De Boor, C. On calculating with B-splines. *J. Approx. Theory* **1972**, *6*, 50–62. [CrossRef]

43. Elósegui, P.; Ruis, A.; Davis, J.; Ruffini, G.; Keihm, S.; Bürki, B.; Kruse, L. An experiment for estimation of the spatial and temporal variations of water vapor using GPS data. *Phys. Chem. Earth* **1998**, *23*, 125–130. [CrossRef]

44. Magee, L. Nonlocal Behavior in Polynomial Regressions. *Am. Stat.* **1998**, *52*, 20. [CrossRef]

45. Amerian, Y.; Voosoghi, B.; Hossainali, M.M. Regional ionosphere modeling in support of IRI and wavelet using GPS observations. *Acta Geophys.* **2013**, *61*, 1246–1261. [CrossRef]

46. Hardy, B. ITS-90 Formulations for Water Vapor Pressure, Frostpoint Temperature, Dewpoint Temperature, and Enhancement Factors in range −100 to +100 C. In Proceedings of the Third International Symposium on Humidity and Moisture, Teddington, UK, 6–8 April 1998; pp. 1–8.

47. Mateus, P.; Mendes, V.; Plecha, S. HGPT2: An ERA5-Based Global Model to Estimate Relative Humidity. *Remote Sens.* **2021**, *13*, 2179. [CrossRef]

48. Hansen, P.C. *Rank-Deficient and Discrete Ill-Posed Problems. Numerical Aspects of Linear Inversion, Monographs on Mathematical Modeling and Computation*; SIAM: Philadelphia, PA, USA, 1997; Volume 4.

49. Haji-Aghajany, S.; Voosoghi, B.; Amerian, Y. Estimating the slip rate on the north Tabriz fault (Iran) from InSAR measurements with tropospheric correction using 3D ray tracing technique. *Adv. Space Res.* **2019**, *64*, 2199–2208. [CrossRef]

50. Haji-Aghajany, S.; Amerian, Y. An investigation of three dimensional ray tracing method efficiency in precise point positioning by tropospheric delay correction. *J. Earth Space Phys.* **2018**, *44*, 39–52. [CrossRef]

51. Abdelwares, M.; Haggag, M.; Wagdy, A.; Lelieveld, J. Customized framework of the WRF model for regional climate simulation over the Eastern NILE basin. *Arch. Meteorol. Geophys. Bioclimatol. Ser. B* **2017**, *134*, 1135–1151. [CrossRef]

52. Rahman Hashmi, M.Z.U.; Shamseldin, A.Y.; Melville, B.W. Comparison of MLP-ANN Scheme and SDSM as Tools for Providing Downscaled Precipitation for Impact Studies at Daily Time Scale. *J. Earth Sci. Clim. Chang.* **2018**, *9*, 1–4. [CrossRef]

53. Wilby, R.; Hay, L.; Leavesley, G. A comparison of downscaled and raw GCM output: Implications for climate change scenarios in the San Juan River basin, Colorado. *J. Hydrol.* **1999**, *225*, 67–91. [CrossRef]

54. Wilby, R.L.; Tomlinson, O.J.; Dawson, C. Multi-site simulation of precipitation by conditional resampling. *Clim. Res.* **2003**, *23*, 183–194. [CrossRef]

55. Haykin, S. *Neural Networks: A Comprehensive Foundation*, 2nd ed.; Prentice-Hall: Englewood Cliffs, NJ, USA; New York, NY, USA, 1999.

56. Ahmed, K.; Shahid, S.; Bin Haroon, S.; Xiao-Jun, W. Multilayer perceptron neural network for downscaling rainfall in arid region: A case study of Baluchistan, Pakistan. *J. Earth Syst. Sci.* **2015**, *124*, 1325–1341. [CrossRef]

57. Hornik, K.; Stinchcombe, M.; White, M. Multilayer feed forward networks are universal approximates. *Neural Netw.* **1989**, *2*, 359–366. [CrossRef]

58. Levenberg, K. A method for the solution of certain non-linear problems in least squares. *Q. Appl. Math.* **1944**, *2*, 164–168. [CrossRef]

59. Marquardt, D.W. An Algorithm for Least-Squares Estimation of Nonlinear Parameters. *J. Soc. Ind. Appl. Math.* **1963**, *11*, 431–441. [CrossRef]

60. Banerjee, P.; Prasad, R.K.; Singh, V.S. Forecasting of groundwater level in hard rock region using artificial neural network. *Environ. Earth Sci.* **2008**, *58*, 1239–1246. [CrossRef]

61. Chang, J.; Wang, G.; Mao, T. Simulation and prediction of supra permafrost groundwater level variation in response to climate change using a neural network model. *J. Hydrol.* **2015**, *529*, 1211–1220. [CrossRef]

62. Moriasi, D.N.; Arnold, J.G.; van Liew, M.W.; Bingner, R.L.; Harmel, R.D.; Veith, T.L. Model evaluation guidelines for systematic quantification of accuracy in watershed simulations. *Trans. ASABE* **2007**, *50*, 885–900. [CrossRef]

63. Hersbach, H.; Dee, D. *ERA5 Reanalysis is in Production; ECMWF Newsletter 147*; ECMWF: Reading, UK, 2016.

64. Haji-Aghajany, S.; Amerian, Y. Atmospheric phase screen estimation for land subsidence evaluation by InSAR time series analysis in Kurdistan, Iran. *J. Atmos. Sol. Terr. Phys.* **2020**, *205*, 105314. [CrossRef]

65. Haji-Aghajany, S.; Amerian, Y. Assessment of InSAR tropospheric signal correction methods. *J. Appl. Remote Sens.* **2020**, *14*, 044503. [CrossRef]

66. Aghajany, S.H.; Voosoghi, B.; Yazdian, A. Estimation of north Tabriz fault parameters using neural networks and 3D tropospherically corrected surface displacement field. *Geomat. Nat. Hazards Risk* **2017**, *8*, 918–932. [CrossRef]

67. Dach, R.; Lutz, S.; Walser, P.; Fridez, P. (Eds.) *Bernese GNSS Software Version 5.2. User Manual*; Astronomical Institute, University of Bern; Bern Open Publishing: Bern, Switzerland, 2015; ISBN 978-3-906813-05-9. [CrossRef]

68. Böhm, J.; Niell, A.; Tregoning, P.; Schuh, H. Global Mapping Function (GMF): A new empirical mapping function based on numerical weather model data. *Geophys. Res. Lett.* **2006**, *33*, 1–4. [CrossRef]